NEUROSCIENCE

Dendritic synapse geometry optimizes binaural computation in a sound localization circuit

Rei Yamada and Hiroshi Kuba*

Clustering of synapses allows neurons to overcome attenuation of electrical signals at dendrites. However, we show in avian binaural coincidence detectors computing interaural time difference for sound localization that clustering of synapses rather promotes the dendritic attenuation but augments the intensity tolerance of the binaural computations. Using glutamate uncaging, we found in the neurons that synapses were clustered at distal dendritic branches. Modeling revealed that this strengthened sublinear integration within a dendritic tree but enabled the integration of signals from different trees when inputs grow stronger, preventing monoaural output and maintaining the dynamic range of binaural computation. The extent of this clustering differed according to dendritic length and frequency tuning of neurons, being most prominent for long dendrites and low-frequency tuning. This ensures binaural spatial hearing for wide intensity and frequency ranges, highlighting the importance of coupling of synapse geometry with dendritic morphology and input frequency in sensory signal processing.

INTRODUCTION

The integration of signals generated by a neuron's different synaptic inputs is intrinsically nonlinear. Such nonlinearities have a strong impact on the input-output relationship of neurons, and they are sensitive to the precise distribution of synapses along dendrites as well as the dendritic morphology. Distribution of synapses within dendrites is strategically determined in individual neurons (*1*). In pyramidal neurons, which have thick and active dendrites, closely clustered synapses promote supralinear integration via activation of voltage-gated channels and *N*-methyl-D-aspartate (NMDA) receptors, facilitating the spike output of the neurons. On the other hand, sparse distribution of synapses is favorable in facilitating the output in neurons with thin and passive dendrites. However, the computational roles of synapse distribution and their relationship to dendritic morphology are not fully understood.

Auditory coincidence detection is the neuronal basis of encoding interaural time differences (ITDs) for sound source localization. In birds, neurons in nucleus laminaris (NL) that receive excitatory inputs from bilateral cochlear nucleus change firing in a manner dependent on ITDs, mediating their well-known coincidence detection (Fig. 1A) (*2*). NL is organized tonotopically, such that the tuning frequency [characteristic frequency (CF)] of neurons increases in a caudolateral-to-rostromedial direction (Fig. 1B) (*3*). In addition, the neurons are biophysically and morphologically differentiated along the tonotopic axis, ensuring coding of ITDs across frequencies (*4*). For example, NL neurons extend aspiny dendrites in the ventral and dorsal directions, and the length of the dendrites increases with a decrease of CF (*5*). Moreover, each dendrite receives inputs from only one side, ventral dendrites receiving contralateral signals and the dorsal dendrites receiving ipsilateral signals, thus segregating input sources within a single cell. Simulation studies proposed that this segregation is advantageous for the ITD tuning (*6*), but detailed information on the synapse location is lacking and the roles of dendritic computation in the ITD coding remain elusive.

Department of Cell Physiology, Nagoya University, Graduate School of Medicine, Nagoya 466-8550, Japan.
*Corresponding author. Email: kuba@med.nagoya-u.ac.jp

In this study, we found in chicken NL neurons that synapses were clustered at distal thin dendritic branches, which strengthened the attenuation of synaptic responses within a dendritic tree via facilitating sublinear integration, thereby improving binaural computation for strong inputs. The extent of this clustering was determined optimally according to dendritic length and CF of neurons; it was prominent for neurons with longer dendrites and lower CF, suggesting that the coupling of synapse geometry with dendritic morphology and input frequency is a mechanism to ensure the accurate ITD tuning for wide intensity and frequency ranges.

RESULTS

Tonotopic region–specific distribution of glutamate receptors at dendrites

To reveal the functional distribution of excitatory inputs, we activated glutamate receptors in discrete regions along a dendrite of NL neurons in acute brain slices of chickens using focal uncaging of glutamate with either single-photon or two-photon stimuli. Current amplitude was monitored at soma with Cs^+-based internal solution. The usage of the two uncaging strategies allowed the evaluation of receptor density in different unit lengths of the dendrite (Fig. 1C and fig. S1). In low-CF neurons, the single-photon stimuli caused a faint current response at the proximal trunk (positions 1 to 4), but the response size increased sharply at the distal dendritic regions (positions 5 to 8), where many thin branches appeared (Fig. 1D). This tendency was similar in other low-CF neurons; overall, the response was ~10 times larger at distal branches (>80%, red circles) than at proximal trunks (<20%, blue circles) (Fig. 1, E and F). However, a possibility remained that the wide area of single-photon stimulation contributed to the regional difference of the responses along the dendrites, because the density of dendrites may increase at the distal area because of the extensive branching of dendrites. Therefore, we evaluated the receptor density with two-photon uncaging that illuminates a more limited area. Even with the two-photon uncaging, response size was five times larger at the distal dendrites (Fig. 1, G to I), confirming that the density of glutamate receptors was elevated at distal thin dendrites in low-CF neurons. In high-CF neurons, the single-photon stimuli caused a substantial

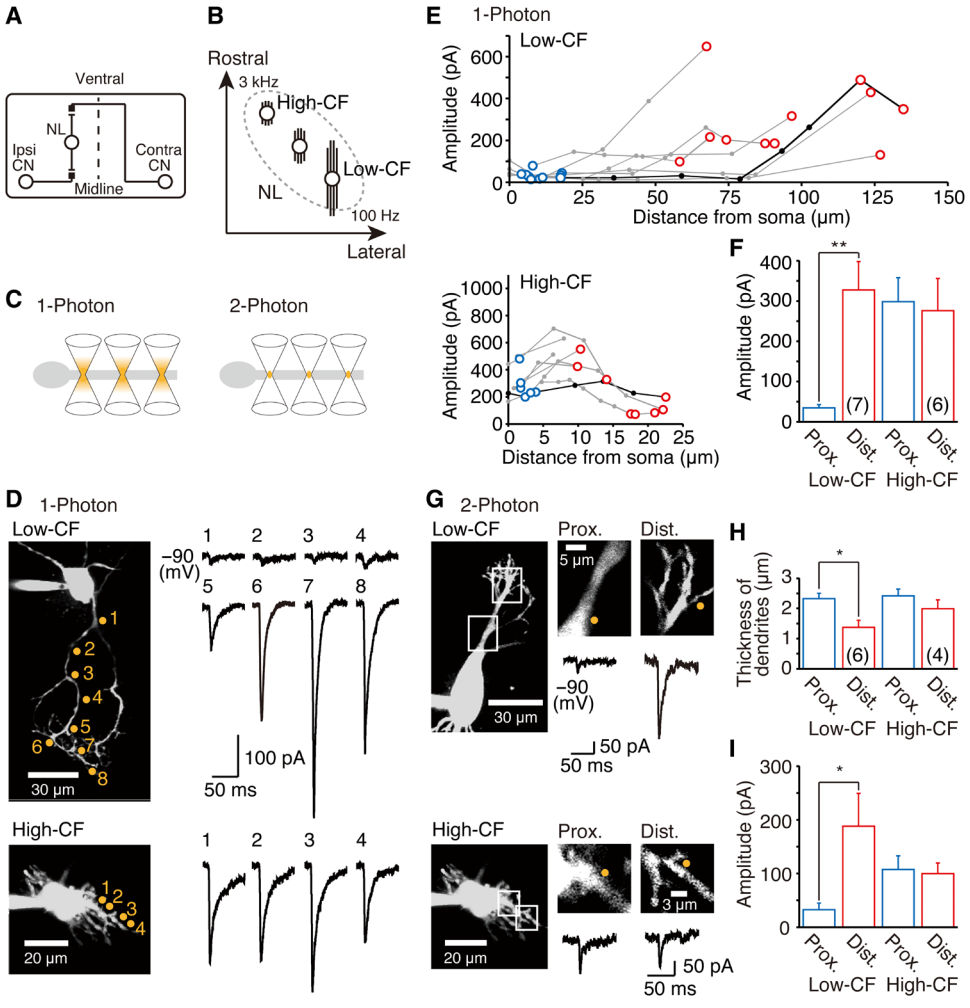

Fig. 1. Biased distribution of glutamate receptors at dendrites in low-CF neurons. (**A**) Brainstem auditory circuit of chickens. CN, cochlear nucleus. (**B**) Tonotopic organization of NL. (**C**) Schematic drawing of single- and two-photon stimulation. (**D**) Single-photon (405 nm) glutamate uncaging along dendrites in low-CF and high-CF neurons. Current responses at soma are shown for corresponding uncaged points (orange). (**E**) Current amplitude against distance from soma for seven dendrites of low-CF neurons and six dendrites of high-CF neurons. Data in (D) are connected with black lines. Blue and red circles indicate responses from proximal (<20% of length) and distal (>80%) locations, respectively. (**F**) Current amplitude by single-photon stimuli. (**G**) Two-photon (720 nm) glutamate uncaging in low-CF and high-CF neurons. Proximal and distal dendrites are magnified, and current responses from each location (orange) are shown. (**H**) Thickness of stimulated dendrites. (**I**) Current amplitude by two-photon stimuli. **P* < 0.05 and ***P* < 0.01 in this figure and in subsequent figures.

response irrespective of the location (Fig. 1, D to F), and the tendency was the same for the two-photon stimuli (Fig. 1, G to I). These indicated that glutamate receptors and presumably synapses were distributed more uniformly along dendrites in high-CF neurons, which may support the previous electron microscopic results of synapse density in short dendrites (*7*).

Decay phase of uncaging currents was fitted by a double exponential function (fig. S2). Because the slower component remained in the presence of 2-amino-5-phosphonovaleric acid (AP-5) (100 μM, NMDA receptor antagonist) in the bath, contributions of NMDA receptors to the component would be small. Given that the decay kinetics of uncaging currents is determined by the position of uncaging spot relative to synapses, lifetime of uncaged glutamate, and kinetics of receptors, the slower decay component could be attributed to the activation of nearby receptors by diffused glutamate.

Excitatory synapses were clustered at distal dendrites in low-CF neurons

We next determined whether this skewed receptor density in the low-CF neurons is due to an increase in synapse density or in receptor density at individual synapses. We recorded miniature excitatory postsynaptic currents (mEPSCs) at the soma while applying a high-osmotic solution focally around proximal or distal dendrites through a pipette to trigger local exocytosis from synapses (Fig. 2A). The high-osmotic stimulation increased the frequency of mEPSCs by two to six times in both regions, while the amplitude of mEPSCs did not differ between the regions (Fig. 2, A and B). This indicated that the density of glutamate receptors does not differ for different synapses along the dendrite, suggesting that the skewed receptor distribution revealed by uncaging is due to an accumulation of synaptic terminals at distal dendrites in the low-CF neurons. Notably,

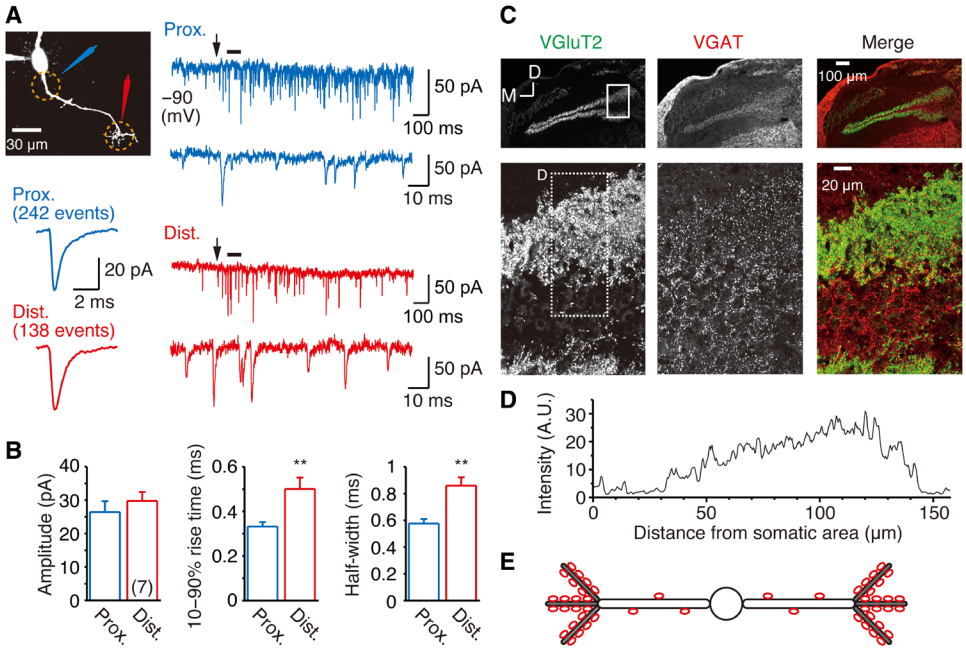

Fig. 2. Excitatory synapses would be accumulated at distal dendrites in low-CF neurons. (**A**) mEPSCs evoked by puff application of sucrose to proximal (blue) and distal (red) dendrites in a low-CF neuron. Arrows indicate onset of application, black bars (100 ms) are magnified, and mEPSCs are ensemble-averaged for 500 ms. (**B**) Amplitude, rise time, and half-amplitude width of mEPSCs from seven cells. The similar mEPSC amplitude indicated that receptor density at individual synapses would not differ between proximal and distal dendrites, further suggesting that the larger current at distal dendrites in two-photon uncaging would reflect an increase of synapse density at the distal region. (**C**) Confocal images of VGluT2 (green) and VGAT (red) immunosignals in coronal section of NL. Boxes are magnified. (**D**) Average intensity profile of VGluT2 signals at the region surrounded by the dotted line in (C). Note an increasing tendency for VGluT2 signals at the distal region. A.U., arbitrary units. (**E**) Excitatory synapses would be concentrated at distal thin branches in low-CF neurons.

vesicular glutamate transporter 2 (VGluT2)–positive excitatory terminals were restricted to ventral and dorsal dendritic layers, which contrasted to the vesicular γ-aminobutyric acid transporter (VGAT)–positive inhibitory terminals at the somatic layer. Moreover, they were more separated at the lateral low-CF region of NL, and their intensity profile showed a mild increasing tendency around the distal dendritic areas (Fig. 2, C and D). These results might support the electrophysiological results that excitatory synapses were clustered at the distal thin part of long dendrites in the low-CF neurons (Fig. 2E).

Attenuation of uncaging potentials at distal dendrites of low-CF neurons

The impact of synapse distribution was evaluated by recording membrane potential at the soma with K^+-based internal solution while applying single-photon stimuli of a constant intensity to dendrites in low-CF neurons (Fig. 3, A to E). The maximum voltage responses occurred at distal dendrites, but the size was larger than that at proximal dendrites by only two to three times, which was far smaller than the difference of current responses (Fig. 1). In addition, these responses were accelerated and accompanied by a rapid after-hyperpolarization. Moreover, when the intensity of single-photon stimuli was elevated, the uncaging potentials increased at both dendritic regions, but this increase was more prominent under the blockade of K^+ channels with Cs^+-based internal solution specifically at distal regions and strong intensities (Fig. 3, F to I). These results confirmed that voltage-gated K^+ channels were strongly activated by uncaging potentials and contributed to the intensity-dependent attenuation (i.e., sublinear summation) of uncaging potentials at the distal dendrites. On the other hand, depolarizing active currents would not be activated by the uncaging potentials irrespective of dendritic regions, because blockers of these currents, such as tetrodotoxin (TTX) (1 μM, Na^+ channel blocker), TTA-P2 (2 μM, T-type Ca^{2+} channel blocker), and AP-5 (100 μM), did not affect the uncaging potentials (Fig. 3H).

We next examined the characteristics of integration at distal dendrites in a finer scale by uncaging glutamate with the two-photon stimuli (Fig. 4, A to D). We stimulated multiple points (eight points) along a short stretch of dendrite (~15 μm) quasi-simultaneously or individually and compared the responses for the two patterns of stimuli. The results showed that the quasi-simultaneously induced (i.e. spatially summated) response was apparently smaller than the arithmetic sum of individual responses, indicating that sublinear summation occurred at the distal dendritic regions. Thus, the integration at distal dendrites of low-CF NL neurons would be, in principle, sublinear. However, there were limitations in controlling spatiotemporal patterns of inputs in brain slices, and therefore, we further examined the mechanism and significance of synapse clustering in a model of the low-CF NL neurons.

Synaptic clustering at distal dendrites augmented sublinear integration

The model neuron had a long dendrite (100 μm with 10 compartments), and synaptic inputs were either distributed along the length of the dendrite or tightly clustered in the distal region (Fig. 5, A and B). Synaptic potentials increased sublinearly with an increase in the input conductance, but the sublinearity differed between the

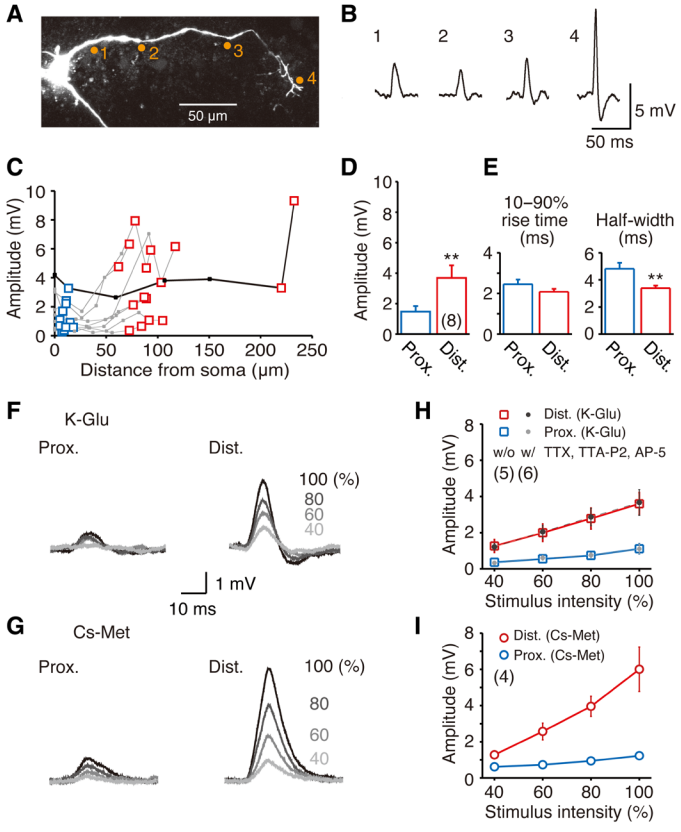

Fig. 3. Intensity-dependent attenuation of uncaging potentials at distal dendrites in low-CF neurons. (**A** and **B**) Single-photon glutamate uncaging along a dendrite in a low-CF neuron. Voltage responses were recorded at soma with K^+-based internal solution. Uncaged points are shown (orange). (**C**) Voltage amplitude against distance from soma for eight cells. The black line indicates data in (A). Blue and red squares indicate responses from proximal (<20% of length) and distal (>80%) locations, respectively. (**D** and **E**) Amplitude, 10 to 90% rise time and half-amplitude width of uncaging potentials. (**F** and **G**) Somatic responses to uncaging at proximal and distal dendrites with different intensities. K^+-based (F) and Cs^+-based (G) internal solutions. Uncaging intensity was increased by elevating laser power from 40 to 100% with a 20% step. (**H** and **I**) Amplitude of somatic responses against uncaging intensity (40 to 100%). Without (open squares) and with (gray dots) TTX (1 μM), TTA-P2 (2 μM), and AP-5 (100 μM) in the bath in (H).

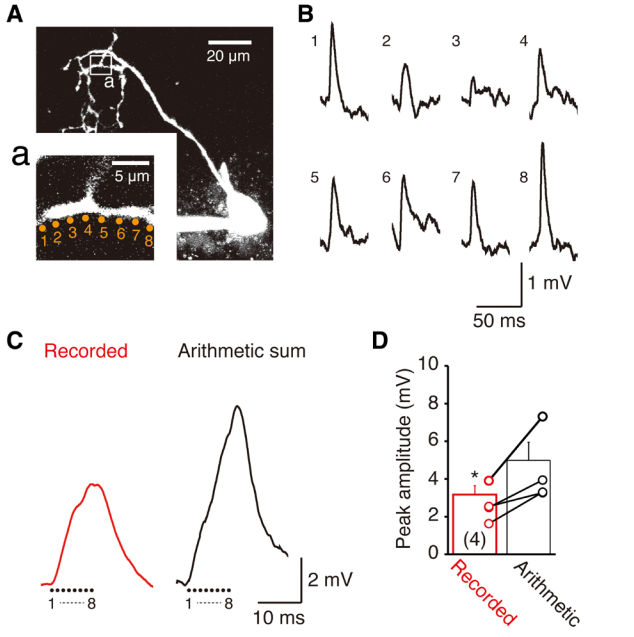

Fig. 4. Sublinear integration of uncaging potentials at distal dendrites in low-CF neurons. (**A** and **B**) Two-photon glutamate uncaging (1-ms duration) at eight points (orange) along a short stretch of dendrite (~15 μm) in a low-CF neuron and corresponding voltage responses recorded at soma with K^+-based internal solution. Each point was separated by >1 μm to avoid stimulating the same receptors repeatedly. (**C**) Response by quasi-simultaneous stimuli to the points (interpulse interval of 0.3 ms) (red) and arithmetic sum of individual responses at the same interval (black). Note that the recorded response was 56% smaller than the arithmetic sum, indicating that sublinear integration occurred at the distal dendritic compartment. (**D**) Peak amplitude of quasi-simultaneously induced response and arithmetic sum of individual responses. Duration of uncaging was either 1 or 2 ms.

models depending on the location; the sublinearity was weaker (i.e., more linear) at the input site for distally clustered inputs than for diffusely distributed inputs, while this pattern was reversed and the sublinearity became stronger for the distally clustered inputs when monitored at the soma (Fig. 5, D and E). This difference occurred because the synaptic clustering augmented the local depolarization, having had two consequences: activation of a low-voltage–activated K^+ current (I_{klva}), which shunted excitatory signals, and suppression of synaptic current (I_{syn}) owing to a decrease of driving force for the glutamate receptors (Fig. 5F). These shunting and ceiling effects reduced the net charges at the input site and hence the charges reaching the soma, particularly when the input conductance was large, thus enhancing the degree of sublinearity at the soma. The electrical compactness of input site was critical for this effect of synapse clustering, because it augmented the local depolarization. The sublinearity increased at the soma when the inputs were clustered at a thinner compartment, whereas it decreased when the inputs were clustered at a proximal compartment (fig. S3). Thus, the synaptic clustering at thin distal parts of long dendrites augmented the local shunting and ceiling effects and maximized the sublinearity of somatic responses, which would enable an intensity-dependent adjustment of spike output in the low-CF neurons.

We also examined the effects of dendritic length on the integration of distally clustered inputs with the model having a short dendrite (20 μm with two compartments; Fig. 5C). The sublinearity was similar at the input site irrespective of dendritic length, but it was weakened at the soma for the short dendrite (Fig. 5, D and E). This weaker effect of clustering occurred because the short dendrite decreased the dissipation of charge during signal propagation to the soma and also because it relieved the loss of charge at the input site due to the modest electrical isolation from the soma (Fig. 5F).

Synaptic clustering at distal dendrites improved low-frequency ITD tuning

We simulated the effects of synapse distribution on the ITD tuning in models equipped with two identical dendrites. NL neurons receive synaptic inputs from each ear separately on different dendrites at a rate corresponding to their CF (*8*). Thus, we mimicked low-frequency-sound stimuli by applying a train of synaptic stimuli to each side of dendrite at 250 Hz and changed the phase between the two sides (Fig. 6, A to D). When diffuse inputs were applied in the model with long dendrites, action potentials appeared with the

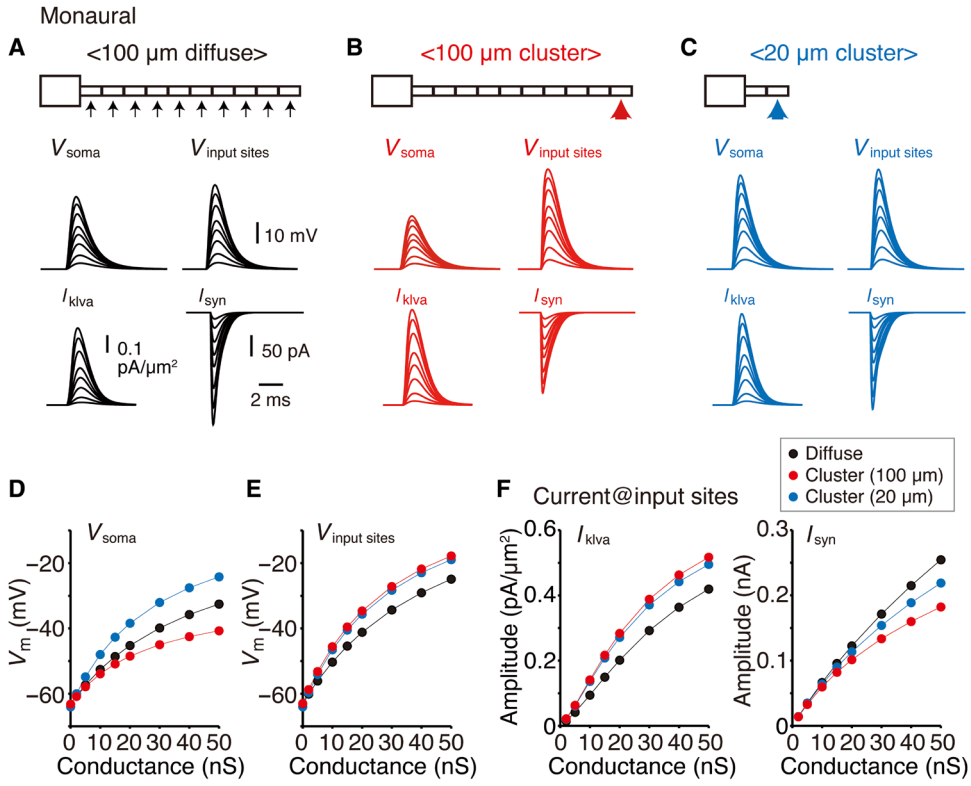

Fig. 5. Distal clustering of synapses facilitated sublinear integration at soma. (**A** to **C**) Synaptic integration in model neurons. Input conductance was increased to mimic the elevation of sound intensity (see Materials and Methods), while it was distributed diffusely along long dendrite (100 μm, A), localized at distal-end compartment (10th) of long dendrite (100 μm, B) and localized at distal-end compartment (2nd) of short dendrite (20 μm, C). For diffuse model, input conductance was divided by 10 and distributed evenly in every compartment. Synaptic potentials at soma and input site, I_{klva} and I_{syn} at input site are superimposed. (**D** to **F**) Amplitudes of synaptic potentials at soma and input site, I_{klva} and I_{syn} at input site against input conductance. For diffuse input, every compartment was averaged. I_{syn} was smaller for the 100-μm dendrite than for the 20-μm dendrite in the clustered input model, because rising phase of synaptic potentials at input site was faster for the 100-μm dendrite owing to an electrical isolation of input site from the soma; 10 to 90% rise time of synaptic potentials at 50 nS was 0.25 and 0.33 ms for the 100- and 20-μm dendrite, respectively.

in-phase stimuli when the input conductance was 11 nS, and they reached the maximum rate level with a slight elevation of the conductance, creating a large ITD contrast. However, a further elevation of the conductance (23 nS) reduced the ITD contrast, because the synaptic inputs increased firing even with the out-of-phase stimuli (Fig. 6B). We then applied distally clustered inputs in the model with long dendrites. The clustered inputs elevated the threshold of firing slightly for the in-phase stimuli (13 nS), but the effect was much larger for the out-of-phase stimuli (30 nS), which maintained the ITD contrast for wider conductance ranges and ensured a substantial dynamic range of ITD tuning (Fig. 6C). In the model with short dendrites, the threshold conductance decreased for both the in-phase (7 nS) and the out-of-phase (13 nS) stimuli and thus showed a narrowed dynamic range (Fig. 6D). These results indicated that the distal clustering of inputs on long dendrites prevented neuronal firing for the out-of-phase stimuli in an intensity-dependent manner, which maintained the dynamic range of ITD tuning for low-frequency stimuli (Fig. 6E).

Stimulus frequency had substantial effects on the ITD tuning; the dynamic range decreased with an increase of the frequency and almost disappeared at 1 kHz in the models with long dendrites (Fig. 6F and fig. S4). Accordingly, the synaptic clustering no longer maintained the dynamic range of ITD tuning at a stimulus frequency higher than 500 Hz. This occurred because the threshold of firing for binaural stimuli decreased at higher frequencies, while the extent was much larger for the out-of-phase stimuli (fig. S4, A, B, E, and F), diminishing the difference of firing between the in-phase and the out-of-phase stimuli. Thus, the combination of long dendrites and distal synaptic clustering are particularly important for the ITD tuning of low-frequency sound. Of note, the model with short dendrites could not maintain the ITD contrast at higher frequencies (fig. S4, C, D, G, and H), because the synaptic current of low-CF neurons, the kinetics of which is much slower than that of high-CF neurons (*4*, *9*), was used in the simulation.

We further explored the mechanisms underlying the frequency-dependent effects of the synaptic clustering by examining voltage responses to a train of synaptic stimuli on a distal dendritic compartment in the model with a long dendrite under a blockade of spike generation (Fig. 7). With an increase in the stimulus frequency, the fluctuating component of I_{syn} became smaller because of a decrease of peak current and an increase of trough current (Fig. 7D). Moreover, the level of temporal summation increased (mean, black broken lines), which further reduced the membrane potential oscillation (fluctuating, black bracket) at the soma (Fig. 7, A and B) due to an increase of I_{klva} at the input site (Fig. 7C), diminishing the differences in the firing responses to the train between the in-phase

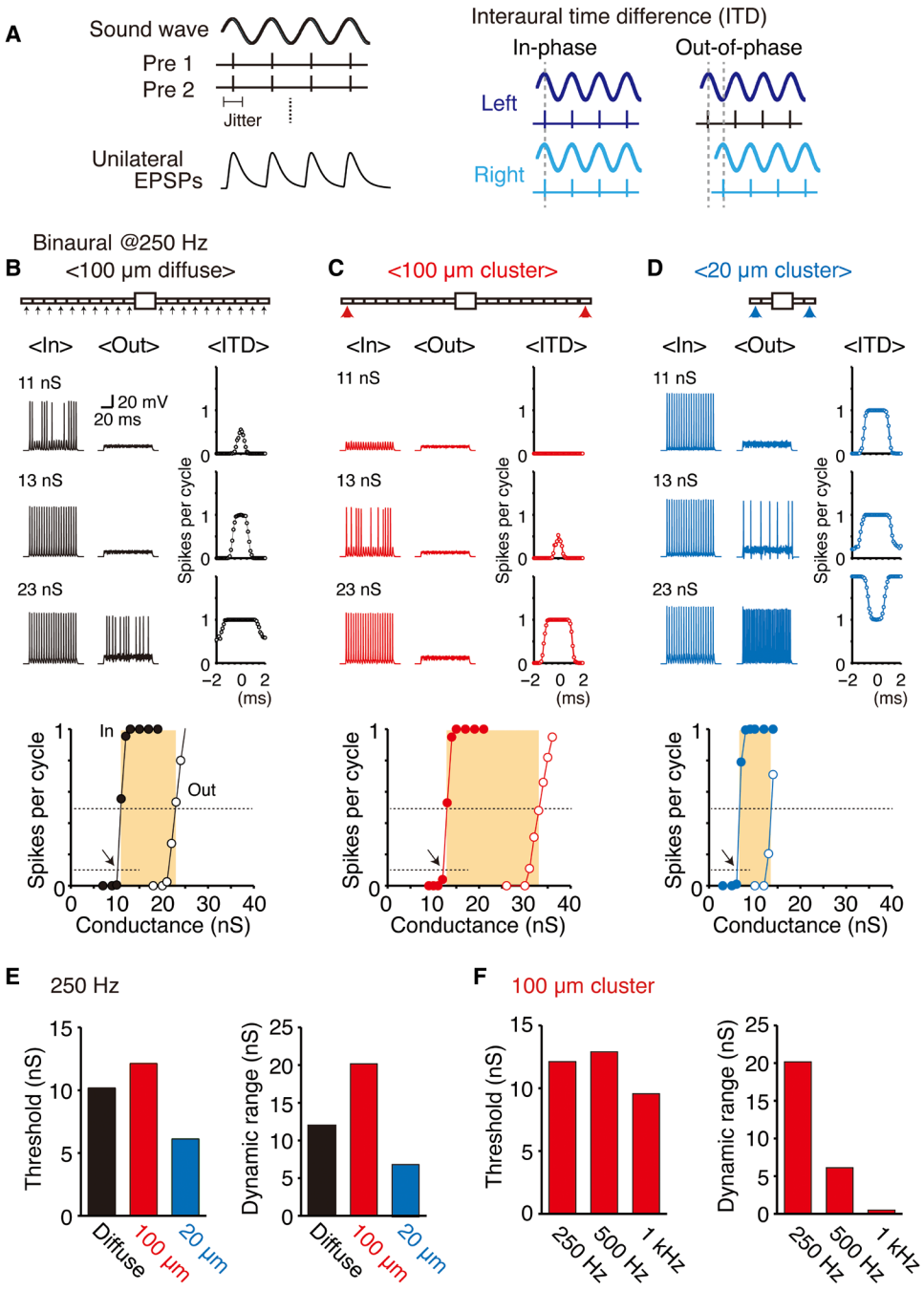

Fig. 6. Distal clustering of synapses improved ITD coding for low-frequency stimuli. (**A**) Schematic drawing of stimulus arrangement for modeling ITD responses. A train of synaptic stimuli (20 cycles) was applied to two dendrites, and the timing between the dendrites was altered to mimic ITD. Input conductance was increased to mimic the elevation of sound intensity (see Materials and Methods). (**B** to **D**) ITD responses to low-frequency stimuli (250 Hz). Input conductance was distributed diffusely along a dendrite or localized at distal-end compartment (top). For diffuse model, input conductance was divided by 10 and distributed evenly in every compartment. Traces at in-phase (0-ms ITD) and out-of-phase (2-ms ITD) and spikes per cycle against ITD (middle). Spikes per cycle at in-phase (filled circles) and out-of-phase (open circles) against input conductance at each dendrite (bottom). Arrows and shades indicate threshold and dynamic range of ITD responses, respectively. (**E**) Effects of synapse distribution and dendritic length on threshold and dynamic range of ITD responses at 250 Hz. (**F**) Effects of frequency for distally clustered inputs at long dendrites.

and the out-of-phase stimuli (fig. S4). In support, when we made two-photon glutamate uncaging at multiple points sequentially in a distal dendritic region of actual low-CF NL neurons, the extent of temporal summation became larger at higher frequencies (i.e., shorter time interval of uncaging stimuli) (fig. S5).

DISCUSSION

Excitatory synapses were clustered at distal dendritic branches in low-CF NL neurons. We used single-photon and two-photon stimuli for glutamate uncaging in evaluating the synapse distribution, which we believe to be advantageous for reliable estimates of the

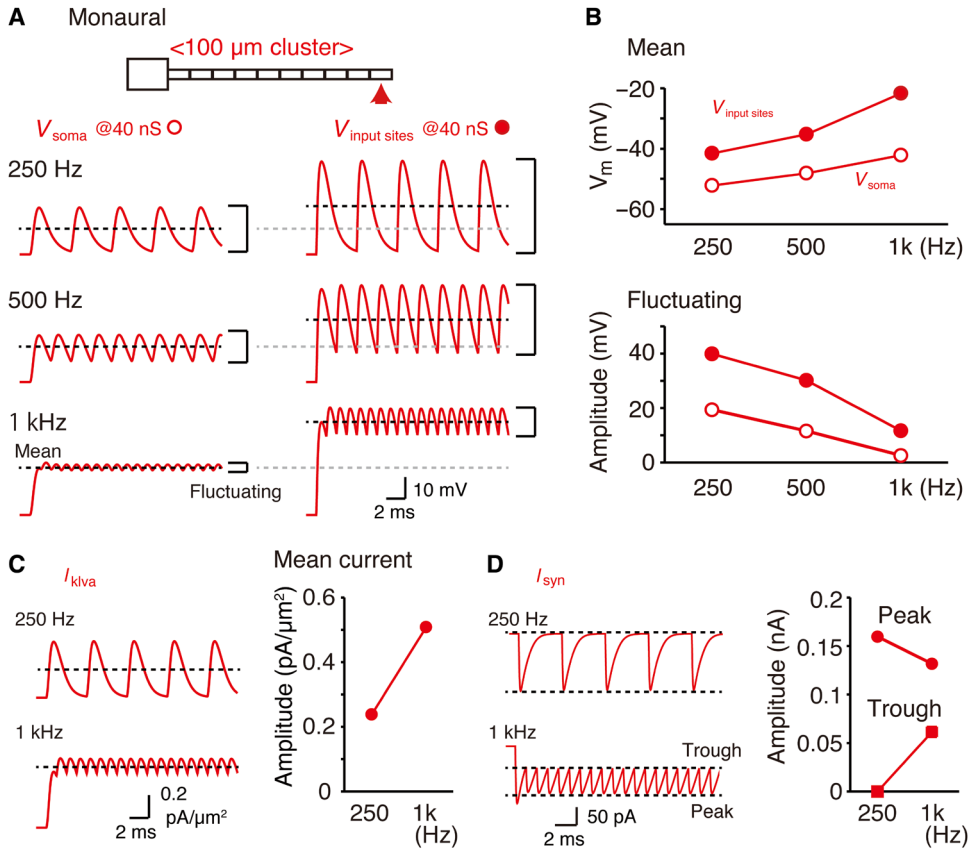

Fig. 7. High-frequency stimuli attenuated fluctuating voltage responses in part due to loss of charges at input site for distally clustered synapses. (**A**) Synaptic potentials by a train of 20 stimuli (40 nS) applied to a dendrite under the blockade of spike generation by setting gNa at 0 S/cm^2. Input conductance was localized at the distal-end compartment (10th) of long dendrite (100 μm), while frequency of stimuli was altered. 250 Hz (top), 500 Hz (middle), and 1 kHz (bottom). Mean depolarization and fluctuating components are indicated by dotted lines and brackets, respectively. (**B**) Mean [dotted lines in (A)] and fluctuating component [brackets in (A)] of depolarization at soma and input site against frequency. (**C** and **D**) I_{klva} and I_{syn} at input site during the stimuli (40 nS) for 250 Hz (top) and 1 kHz (bottom).

distribution at each dendritic region. In particular, NL neurons do not have spines and synapses are directly formed on dendrites. Therefore, the single-photon stimuli, which stimulate a substantial length (10 to 15 μm) of a dendrite, would enable to estimate the synapse distribution at the region rather globally under minimal effects of possible heterogeneity of synapse distribution. On the other hand, the two-photon stimuli, which stimulate a more restricted length (1 to 3 μm), would allow the estimation of the maximum density of synapses locally at the region. The two-photon responses at the proximal region were similar in size to mEPSCs in the low-CF neurons. Therefore, we assumed that the proximal responses reflected the activation of a single synapse and calculated the synapse density at the distal region in the low-CF neurons from the current-distance relationship of the two-photon stimuli (fig. S1). Because the responses at the distal region were about five times larger than those at the proximal region, the calculated density was three to five synapses in 1 μm, which was high compared with those reported in other brain regions (*10*, *11*).

Passive properties of dendrites attenuate synaptic potentials (*1*), while synaptic clustering in principle counteracts this effect. For example, in the hippocampus, an increase of synaptic density toward the distal ends of dendrites compensates for the attenuation of synaptic potentials, equalizing their impact on the soma (*12*, *13*). Another example is clustering of functionally correlated synapses (*14*), which can augment the depolarization at dendrites via activating active conductances, such as Na^+ channels, Ca^{2+} channels, and NMDA receptors (*15*). This supralinear integration increases the impact of spatiotemporally correlated inputs on the soma, creating multiple functional units within dendrites, and is proposed to underlie the perception of sensory signals in the cortex (*16*–*18*) or the representation of place field in the hippocampus (*19*).

Synaptic clustering had unique and distinct effects on neuronal computation in low-CF NL neurons; it augmented the local depolarization specifically for correlated inputs from the same ear, but it weakened their impact on the soma by facilitating sublinear integration, which would prevent the firing by monaural inputs (i.e., monaural coincidence detection). Supportively, supralinear conductances were weak or absent at dendrites of NL neurons; functional NMDA receptors are almost lost before hatch (*20*) despite their substantial expressions of mRNA and protein (*21*, *22*), and activation of Ca^{2+} channels is limited at the onset of ongoing input because of their inactivating features (*23*). Because inputs from different ears are summated linearly at the soma (*24*, *25*), this sublinear integration of inputs from the same ear suppresses the firing at the out-of-phase owing to the prolonged activation of K^+ channels during the tonic depolarization. However, this effect is kept weak at the

in-phase during the large oscillatory depolarization (see Fig. 6), which enables ITD calculation (i.e., binaural coincidence detection) for strong inputs and maintains the dynamic range of ITD tuning. This is in line with a dynamic clamp study in NL that the small and multiple synaptic inputs at the soma were proposed to make a large contrast of ITD tuning (i.e., difference of firing between in-phase and out-of-phase) for low-frequency sound (*26*). The contrast of ITD tuning increases with sound intensity, and it is maintained at strong intensity, securing the dynamic range of ITD tuning in NL neurons in vivo (*27*, *28*). This intensity dependence of ITD tuning may primarily reflect that of presynaptic inputs (*29*), but it also requires GABAergic shunting conductance that suppresses firing at the out-of-phase for strong sound (*27*, *30*). Thus, the synapse clustering at distal dendrites together with the GABAergic shunting conductance would adjust the size of individual synaptic inputs at an appropriate level, which would prevent the firing by monaural inputs particularly at the out-of-phase and maintain the ITD tuning against wide intensity ranges of sound in the low-CF neurons in vivo. Notably, the strong sublinearity implies that many synaptic inputs are required to induce substantial depolarization at the soma, suggesting that large energy might be consumed to maintain the ITD tuning for low-frequency sound.

Clustering of synapses at distal locations of long and thin dendrites facilitates sublinearity at the soma and improves the ITD tuning for low-frequency sound (<500 Hz). However, these characteristics of synapse geometry deteriorate the ITD tuning for higher-frequency sound, because they enhance tonic depolarization owing to a robust temporal summation of high-frequency signals at dendrites. Therefore, high-CF neurons minimize the temporal summation via distributing synapses diffusely along short and thick dendrites as well as by having rapid receptor kinetics and large potassium channel expression (*4*, *9*) and thus maintain ITD tuning for higher-frequency sound, indicating that the coupling of synaptic geometry with frequency tuning and dendritic length optimizes binaural computations in NL.

Medial superior olive (MSO) is a mammalian homolog of NL, and ITDs are encoded by neurons with long bipolar dendrites (*31*). In gerbil MSO, the dendrites are composed mostly of a thick trunk with uniform distribution of AMPA receptors (*32*). In addition, the dendrites have large proximal expression of K^+ channels (*33*, *34*). These features maintain the amplitude of synaptic potentials by preventing sublinear integration but accelerate their time course by activating K^+ channels, thereby improving the binaural coincidence detection (*33*, *35*), just as in the higher-CF neurons of chick NL (*4*). ITD coding strategies depend on the head size and input frequencies (*36*). In addition, a large variation exists for the dendritic morphology of MSO neurons among species, and extensive thin branches are observed at the distal end in many mammals [cat (*37*), ferret (*38*), and guinea pig (*31*)]. Thus, the present finding in NL may also provide important insights into the principles of ITD calculation in mammalian species.

MATERIALS AND METHODS

Slice preparation and electrophysiology

The animals were maintained and treated according to the Animal Research Committee of Nagoya University. The brain slices were prepared from chickens (*Gallus gallus domesticus*) of either sex between embryonic day 21 and posthatch day 4. Detailed brain slice preparation and maintenance procedures were described (*39*). During the experiments, the slices were continuously perfused with normal artificial cerebrospinal fluid (ACSF) [125 mM NaCl, 2.5 mM KCl, 26 mM $NaHCO_3$, 1.25 mM NaH_2PO_4, 2 mM $CaCl_2$, 1 mM $MgCl_2$, and 17 mM glucose (pH 7.4)]. The experiments were performed at 31° to 33°C. Whole-cell recordings were performed with Multiclamp 700B (Molecular Devices) under an upright microscope equipped with differential interference contrast optics (BX61WI, Olympus Optical) and an infrared sensitive charge-coupled device camera (C5999, Hamamatsu Photonics). The patch pipettes were fabricated from thin-walled borosilicate glass capillaries (GC150TF-10, Harvard Apparatus) and had resistances of 2 to 5 megohms when filled with Cs^+-based internal solution [140 mM Cs-methanesulfonate, 20 mM CsCl, 0.2 mM EGTA, and 10 mM Hepes (pH 7.2)] or K^+-based internal solution [160 mM K-gluconate, 0.2 mM EGTA, and 10 mM Hepes-KOH (pH 7.2)]. The electrode capacitance was compensated electronically, and the series resistance (<10 megohms) was compensated by 60 to 80%. The liquid junction potential (10 mV) was corrected after the experiments. In all experiments, SR95531 (10 μM; Abcam) was applied to the bath to block inhibitory synaptic transmission. In voltage-clamp experiments, CsCl (2 mM) was applied to the bath to block the leak conductance through the hyperpolarization-activated cyclic nucleotide-gated cation (HCN) channels (*40*). The data were sampled at 100 kHz and were low-pass–filtered at 10 kHz. Off-line analysis of the data was performed with commercially available software (AxoGraph).

Focal induction of mEPSCs was made by a puff application of a high-osmotic solution (150 mM sucrose in normal ACSF) (*41*) through a pipette (Fig. 2A). The pressure was controlled manually by monitoring the spread of fluorescent dye (Alexa Fluor 594, 20 μM) in the puff solution, and the area was limited within the circle of 30 μm diameter. The recordings were repeated five times, and more than 100 events were collected for 500 ms from each stimulus position.

Glutamate uncaging

Dendrite imaging and glutamate uncaging were performed using an FV1000-MPE laser-scanning microscope system attached to an upright microscope (BX61WI, Olympus) through 25× 0.9–numerical aperture objective (XLPlanN, Olympus). A Ti:sapphire-pulse laser (Maitai HP DeepSee, Spectra Physics) was connected to the microscope. For visualizing the structure of recording neuron, Alexa Fluor 594 dye that was applied to the internal solution (20 μM) was scanned with an 810-nm laser beam. Fluorescence signal was captured through an objective, split into red channel using dichroic mirror (SDM570) and bandpass filter (495 to 540 nm), and then focused on a photomultiplier tube. For glutamate uncaging, the caged compound (MNI-caged-L-glutamate, Tocris Bioscience) was applied to the external ACSF solution at a concentration of 1 to 5 mM. Photostimulation was performed with a 405-nm laser (single-photon) or a 720-nm pulsed laser (two-photon) through a dichroic mirror (FV10-NDMVBY/IR, 405/473-488/559/IR) with 1- to 3-ms duration. Because of the sharp spatial resolution of two-photon uncaging, responses from 8 to 10 spots (<1-μm interval) were recorded at each position, and a maximum response was chosen at the voltage-camp experiments in Fig. 1. Intensity dependence of uncaging potentials was evaluated with single-photon stimuli, because higher intensity (>20%) of two-photon laser stimuli frequently damaged the illuminated dendrites.

Data acquisition and analysis

The CF of each neuron was predicted from the mediolateral localization within the nucleus in coronal slices according to descriptions obtained from previous studies (*3*, *4*). We classified NL into three divisions and analyzed the neurons in rostral one-third as high-CF and caudal one-third as low-CF neurons. The data are given as the mean ± SEM (n = number of cells). Statistical significance was tested with Student's paired t test.

Immunohistochemistry

Mouse monoclonal VGluT2 antibody (2.5 μg/ml; UC Davis), and rabbit polyclonal VGAT antibody (2.5 μg/ml; Synaptic Systems) were used for immunohistochemistry. Chicks were perfused transcardially with a periodate-lysine-paraformaldehyde fixative (ml/g body weight): 1% (w/v) paraformaldehyde, 2.7% (w/v) lysine HCl, 0.21% (w/v) $NaIO_4$, and 0.1% (w/v) Na_2HPO_4. The brainstem was post-fixed for 1.5 hours at 4°C. After cryoprotection with 30% (w/w) sucrose in phosphate-buffered saline, coronal sections (20 to 30 μm) were obtained. The sections were incubated overnight with the primary antibodies and then with Alexa-conjugated secondary antibodies (10 μg/ml; Molecular Probes) for 2 hours and were observed under a confocal laser-scanning microscope (FV1000, Olympus).

Model simulation

Neuronal modeling and simulation were performed with the NEURON 7.4 as described previously (*30*). The model consists of multiple sections: a soma (20 μm in length and 10 μm in diameter) and an axon with a nonmyelinated initial segment (25 μm in length), 10 myelinated internodes, and 10 nodes of Ranvier. We made the dendrite (100 μm in length and 2 μm in diameter) with 10 components (10 μm each), and one or two dendrites were connected to the soma. Hodgkin-Huxley type Na^+ current (*42*), low- and high-voltage–activated K^+ currents (I_{klva} and I_{khva}) (*43*, *44*), and leak current were based on web-accessible Model DB (*45*). K^+ currents and leak current were incorporated into the soma, dendrites, and the initial segment and nodes, whereas Na^+ current was added to the initial segment and nodes of the axon when simulating ITD tuning. Maximum conductance of these currents was based on the previous NL model (*46*), while that of I_{klva} and I_{khva} at the soma and dendrites followed measurements in the low-CF NL neurons (0.002 and 0.001 S/cm^2, respectively) (*4*). We substituted leak current for HCN current, because activation tau of HCN current (>60 ms at −80 mV) was far slower than the half-width of synaptic potentials (1 to 2 ms) (*40*). Temperature was 40°C, and Q_{10} was 3.0. Time step of calculation was 12.5 μs.

Individual excitatory synaptic inputs had a profile of the α function [$= g_{syn}t/\tau_{syn}\exp(1 - t/\tau_{syn})$] with a time constant ($\tau_{syn}$) of 0.32 ms and a conductance of 1 nS, according to the observations in low-CF NL neurons (*4*, *9*). We assumed that the number of inputs in an NL neuron increases with intensity, because the firing rate of presynaptic fibers increases monotonously to a plateau level with sound intensity, while their auditory threshold differs by up to 40 dB among the fibers (*29*), which may imply that the dynamic range of inputs to an NL neuron could be wider than that of presynaptic fibers due to recruitment of higher-threshold fibers at strong intensity. Therefore, we altered input conductance (1 nS × number of inputs) to mimic the elevation of sound intensity (up to 50 nS, from three to five synapses/μm), and it was distributed at the dendrite in different patterns (diffuse versus clustered). When simulating ITD tuning, timing of each input was randomly varied according to the normal distribution with an SD of 0.3 ms, which mimicked the spike jitter of fibers to low-CF NL neurons (*29*). For the simulation of ITD tuning, two identical dendrites were connected to the soma and excitatory synaptic stimuli were applied to each dendrite. Interval of stimuli between the two dendrites was displaced to mimic the ITD. A train of synaptic stimuli (20 cycles) was applied repeatedly, and the number of spikes per cycle was calculated over an average of 10 trials for each ITD. Threshold of ITD tuning was defined as the input conductance of spikes per cycle at in-phase exceeding 0.1, and dynamic range as the input conductance range, where the difference of spikes per cycle between in-phase and out-of-phase was larger than 0.5. Steady and fluctuating components of depolarization during the train were defined as mean and difference of peak and trough of synaptic potentials, respectively.

SUPPLEMENTARY MATERIALS

Supplementary material for this article is available at https://science.org/doi/10.1126/sciadv.abh0024

View/request a protocol for this paper from *Bio-protocol*.

REFERENCES AND NOTES

1. A. Tran-Van-Minh, R. D. Cazé, T. Abrahamsson, L. Cathala, B. S. Gutkin, D. A. DiGregorio, Contribution of sublinear and supralinear dendritic integration to neuronal computations. *Front. Cell. Neurosci.* **9**, 67 (2015).
2. C. E. Carr, M. A. Konishi, A circuit for detection of interaural time differences in the brain stem of the barn owl. *J. Neurosci.* **10**, 3227–3246 (1990).
3. E. W. Rubel, T. N. Parks, Organization and development of brain stem auditory nuclei of the chicken: Tonotopic organization of N. magnocellularis and N. laminaris. *J. Comp. Neurol.* **164**, 411–433 (1975).
4. H. Kuba, R. Yamada, I. Fukui, H. Ohmori, Tonotopic specialization of auditory coincidence detection in nucleus laminaris of the chick. *J. Neurosci.* **25**, 1924–1934 (2005).
5. D. J. Smith, E. W. Rubel, Organization and development of brain stem auditory nuclei of the chicken: Dendritic gradients in nucleus laminaris. *J. Comp. Neurol.* **186**, 213–239 (1979).
6. H. Agmon-Snir, C. E. Carr, J. Rinzel, The role of dendrites in auditory coincidence detection. *Nature* **393**, 268–272 (1998).
7. J. S. Deitch, E. W. Rubel, Rapid changes in ultrastructure during deafferentation-induced dendritic atrophy. *J. Comp. Neurol.* **28**, 234–258 (1989).
8. K. Funabiki, G. Ashida, M. Konishi, Computation of interaural time difference in the owl's coincidence detector neurons. *J. Neurosci.* **31**, 15245–15256 (2011).
9. S. J. Slee, M. H. Higgs, A. L. Fairhall, W. J. Spain, Tonotopic tuning in a sound localization circuit. *J. Neurophysiol.* **103**, 2857–2875 (2010).
10. J. L. Chen, K. L. Villa, J. W. Cha, P. T. So, Y. Kubota, E. Nedivi, Clustered dynamics of inhibitory synapses and dendritic spines in the adult neocortex. *Neuron* **74**, 361–373 (2012).
11. L. K. Parajuli, H. Urakubo, A. Takahashi-Nakazato, R. Ogelman, H. Iwasaki, M. Koike, H. B. Kwon, S. Ishii, W. C. Oh, Y. Fukazawa, S. Okabe, Geometry and the organizational principle of spine synapses along a dendrite. *eNeuro* **7**, ENEURO.0248-20.2020 (2020).
12. J. C. Magee, E. P. Cook, Somatic EPSP amplitude is independent of synapse location in hippocampal pyramidal neurons. *Nat. Neurosci.* **3**, 895–903 (2000).
13. D. A. Nicholson, R. Trana, Y. Katz, W. L. Kath, N. Spruston, Y. Geinisman, Distance-dependent differences in synapse number and AMPA receptor expression in hippocampal CA1 pyramidal neurons. *Neuron* **50**, 431–442 (2006).
14. M. E. Larkum, T. Nevian, Synaptic clustering by dendritic signalling mechanisms. *Curr. Opin. Neurobiol.* **18**, 321–331 (2008).
15. D. Johnston, R. Narayanan, Active dendrites: Colorful wings of the mysterious butterflies. *Trends Neurosci.* **31**, 309–316 (2008).
16. N. L. Xu, M. T. Harnett, S. R. Williams, D. Huber, D. H. O'Connor, K. Svoboda, J. C. Magee, Nonlinear dendritic integration of sensory and motor input during an active sensing task. *Nature* **492**, 247–251 (2012).
17. M. Lavzin, S. Rapoport, A. Polsky, L. Garion, J. Schiller, Nonlinear dendritic processing determines angular tuning of barrel cortex neurons in vivo. *Nature* **490**, 397–401 (2012).
18. S. L. Smith, I. T. Smith, T. Branco, M. Häusser, Dendritic spikes enhance stimulus selectivity in cortical neurons in vivo. *Nature* **503**, 115–120 (2013).
19. M. E. Sheffield, D. A. Dombeck, Calcium transient prevalence across the dendritic arbour predicts place field properties. *Nature* **517**, 200–204 (2015).

20. J. T. Sanchez, Y. Wang, E. W. Rubel, A. Barria, Development of glutamatergic synaptic transmission in binaural auditory neurons. *J. Neurophysiol.* **104**, 1774–1789 (2010).
21. Y. Z. Tang, C. E. Carr, Development of NMDA R1 expression in chicken auditory brainstem. *Hear. Res.* **191**, 79–89 (2004).
22. Y. Z. Tang, C. E. Carr, Development of *N*-methyl-D-aspartate receptor subunits in avian auditory brainstem. *J. Comp. Neurol.* **502**, 400–413 (2007).
23. R. Fukaya, R. Yamada, H. Kuba, Tonotopic variation of the T-type Ca^{2+} current in avian auditory coincidence detector neurons. *J. Neurosci.* **38**, 335–346 (2018).
24. M. van der Heijden, J. A. M. Lorteije, A. Plauška, M. T. Roberts, N. L. Golding, J. G. G. Borst, Directional hearing by linear summation of binaural inputs at the medial superior olive. *Neuron* **78**, 936–948 (2013).
25. T. P. Franken, M. T. Roberts, L. Wei, N. L. Golding, P. X. Joris, In vivo coincidence detection in mammalian sound localization generates phase delays. *Nat. Neurosci.* **18**, 444–452 (2015).
26. A. D. Reyes, E. W. Rubel, W. J. Spain, In vitro analysis of optimal stimuli for phase-locking and time-delayed modulation of firing in avian nucleus laminaris neurons. *J. Neurosci.* **16**, 933–1007 (1996).
27. E. Nishino, R. Yamada, H. Kuba, H. Hioki, T. Furuta, T. Kaneko, H. Ohmori, Sound-intensity-dependent compensation for the small interaural time difference cue for sound source localization. *J. Neurosci.* **28**, 7153–7164 (2008).
28. J. L. Peña, S. Viete, Y. Albeck, M. Konishi, Tolerance to sound intensity of binaural coincidence detection in the nucleus laminaris of the owl. *J. Neurosci.* **16**, 7046–7054 (1996).
29. I. Fukui, T. Sato, H. Ohmori, Improvement of phase information at low sound frequency in nucleus magnocellularis of the chicken. *J. Neurophysiol.* **96**, 633–641 (2006).
30. R. Yamada, H. Okuda, H. Kuba, E. Nishino, T. M. Ishii, H. Ohmori, The cooperation of sustained and phasic inhibitions increases the contrast of ITD-tuning in low-frequency neurons of the chick nucleus laminaris. *J. Neurosci.* **33**, 3927–3938 (2013).
31. P. H. Smith, Structural and functional differences distinguish principal from nonprincipal cells in the guinea pig MSO slice. *J. Neurophysiol.* **73**, 1653–1667 (1995).
32. K. Couchman, B. Grothe, F. Felmy, Functional localization of neurotransmitter receptors and synaptic inputs to mature neurons of the medial superior olive. *J. Neurophysiol.* **107**, 1186–1198 (2012).
33. P. J. Mathews, P. E. Jercog, J. Rinzel, L. L. Scott, N. L. Golding, Control of submillisecond synaptic timing in binaural coincidence detectors by K_v1 channels. *Nat. Neurosci.* **13**, 601–609 (2010).
34. B. D. Winters, S. X. Jin, K. R. Ledford, N. L. Golding, Amplitude normalization of dendritic EPSPs at the soma of binaural coincidence detector neurons of the medial superior olive. *J. Neurosci.* **37**, 3138–3149 (2017).
35. A. R. Callan, M. Heß, F. Felmy, C. Leibold, Arrangement of excitatory synaptic inputs on dendrites of the medial superior olive. *J. Neurosci.* **41**, 269–283 (2021).
36. N. S. Harper, D. McAlpine, Optimal neural population coding of an auditory spatial cue. *Nature* **430**, 682–686 (2004).
37. I. R. Schwarz, Dendritic arrangements in the cat medial superior olive. *Neuroscience* **2**, 81–101 (1977).
38. C. K. Henkel, J. K. Brunso-Bechtold, Dendritic morphology and development in the ferret medial superior olivary nucleus. *J. Comp. Neurol.* **294**, 377–388 (1990).
39. H. Kuba, R. Yamada, H. Ohmori, Evaluation of the limiting acuity of coincidence detection in nucleus laminaris of the chicken. *J. Physiol.* **552**, 611–620 (2003).
40. R. Yamada, H. Kuba, T. M. Ishii, H. Ohmori, Hyperpolarization-activated cyclic nucleotide-gated cation channels regulate auditory coincidence detection in nucleus laminaris of the chick. *J. Neurosci.* **25**, 8867–8877 (2005).
41. J. M. Bekkers, C. F. Stevens, Cable properties of cultured hippocampal neurons determined from sucrose-evoked miniature EPSCs. *J. Neurophysiol.* **75**, 1250–1255 (1996).
42. J. S. Rothman, P. B. Manis, The roles potassium currents play in regulating the electrical activity of ventral cochlear nucleus neurons. *J. Neurophysiol.* **89**, 3097–3113 (2003).
43. M. Rathouz, L. Trussell, Characterization of outward currents in neurons of the avian nucleus magnocellularis. *J. Neurophysiol.* **80**, 2824–2835 (1998).
44. J. Z. Simon, C. E. Carr, S. A. Shamma, A dendritic model of coincidence detection in the avian brainstem. *Neurocomputing* **26-27**, 263–269 (1999).
45. M. L. Hines, T. Morse, M. Migliore, N. T. Carnevale, G. M. Shepherd, ModelDB: A database to support computational neuroscience. *J. Comput. Neurosci.* **17**, 7–11 (2004).
46. H. Kuba, T. M. Ishii, H. Ohmori, Axonal site of spike initiation enhances auditory coincidence detection. *Nature* **444**, 1069–1072 (2006).

Acknowledgments: We thank L. O. Trussell for reading the manuscript. **Funding:** This work was supported by grants-in-aid from MEXT for scientific research (25460285 and 16K08493 to R.Y. and 18H02541 and 19H04747 to H.K.) and grants from the Takeda Science Foundation (to R.Y.). **Author contributions:** R.Y. and H.K. designed and performed experiments, analyzed and discussed data, and wrote the manuscript. All authors approved the manuscript. **Competing interests:** The authors declare that they have no competing interests. **Data and materials availability:** All data needed to evaluate the conclusions in the paper are present in the paper and/or the Supplementary Materials.

Submitted 10 February 2021
Accepted 5 October 2021
Published 24 November 2021
10.1126/sciadv.abh0024